Research on Personalized Aspheric Glasses Design Based on Facial Feature Detection and DLP 3D Printing

Zhuo Zhao, Feilong Jiang, Chuangjia Zhao, Liangjie Xie, Meiqi Wang, Yulu Cheng, Xubao Wang

Abstract—**The purpose of this article is to use 3D printing to improve the refractive power of the eye by using 3D printing to customize glasses that fit the patient's spectacle power. The facial detection method was used to determine the feature point parameters of the patient's eye, and the lens was simulated and verified by the theoretical principle of the Seidel aberration coefficient of the three-order axisymmetric aspheric surface. Subsequently, the SOLIDWORKS modeling software was employed to conduct parametric modeling of the glasses. Eventually, the parametric customization of the glasses was achieved through DLP 3D printers. After the optimization of the aspheric lens, the astigmatism, field curvature and distortion of the whole system have been controlled within a certain range, and the spherical aberration coefficient is significantly reduced after the aspheric treatment. Through 3D printing technology, our team successfully designed a 413-degree myopia glasses. Based on the performance analysis and the results of comfort testing of the final product, it is found that both the optical quality inspection characteristics and the mechanical properties of the product fulfill the stipulated requirements, along with the ergonomic and comfort-related requisites.**

Index Terms—**3D printing, aspheric lenses, myopia glasses, ZEMAX, SOLIDWORKS**

I. Introduction

Nowadays, low vision is one of the common and frequent diseases among children and adolescents in China and in many countries and regions of the world, which seriously affects the healthy growth of children and adolescents. The prevalence of myopia has witnessed a remarkable increase globally. Particularly in Southeast Asian countries, studies have indicated that the prevalence of myopia among young adults reaches as high as 80 to 90 percent, and the prevalence of high myopia is as high as 10 to 20 percent [1]. The prevalence rate of high myopia is as high as 10 to 20 percent. The ocular complications caused by high myopia, such as cataracts, MMD, retinal detachment, glaucoma and so on, will increase substantially [2-3]. The literature suggests that the number of myopes per year increases dramatically. It has been shown that an increase of -1.00D myopia per year increases the risk of MMD by 67% [4]. The risk of MMD increases by 67% with a -1.00D increase in myopia per year. Currently, the design methods of spectacles can be divided into forward design and reverse design. In forward design [5], designers use their own experience and two-dimensional static data of the face to design a series of spectacles with different styles and specifications. Obviously, the designed eyewear cannot take into account the user's facial feature data, and the result of MGWF is not very satisfactory. However, the majority of current methods are based on virtual try-on. Their objective is to improve the visual matching degree between the tried-on glasses and the user, providing convenience for the user's personalized customization in appearance [6-9]. Although there exist several methods that utilize 3D face data, the evaluation of MGWF and the personalization of eyewear remain deficient. There is a lack of a well-established design process, accompanied by long production cycles and exorbitant customization costs. Wearing appropriate myopia glasses can help correct vision and slow down the progression of myopia. Wearing inappropriate glasses can not only fail to correct vision effectively, but may even accelerate the further deterioration of vision, and may also lead to other related health problems.

However, current spectacle lens design commonly uses a 25-degree standard increment in lens grinding, which can't finely customize the refractive index. As a result, patients often get improper lens powers, increasing the risks of vision decline, eye fatigue, etc. Through ZEMAX and SOLIDWORKS simulation of the third-order axisymmetric aspheric lens in this study, astigmatism, field curvature, and spherical aberration are notably reduced. The lens has excellent imaging quality, ensuring a more comfortable wearing experience and better adaptation to individual myopia levels.

Manuscript received September 19, 2024; revised March 4, 2025.

Zhuo Zhao is a postgraduate student at the Beijing University of Technology. Beijing, China,100124. (e-mail: 906464943@qq.com).

Feilong Jiang is a postgraduate student at the Beijing University of Technology. Beijing, China,100124. (e-mail: jfl17880199069@163.com).

Chuangjia Zhao is a postgraduate student at the Beijing University of Technology. Beijing, China,100124. (e-mail: 13709267982@163.com).

Liangjie Xie is a postgraduate student at the Beijing University of Technology. Beijing, China,100124. (e-mail: 1244144922@qq.com).

Meiqi Wang is a postgraduate student at the Beijing University of Technology. Beijing, China,100124. (e-mail: 508188549@qq.com).

Yulu Cheng is a postgraduate student at the Beijing University of Technology. Beijing, China,100124. (e-mail: 2822635743@qq.com).

Xubao Wang is an associate researcher at the Beijing University of Technology. Beijing, China,100124. (corresponding author to provide phone: 13681260829; e-mail: wangxubao@bjut.edu.cn).

II. Methods

A. Face detection

Within the realm of image processing, face detection technology occupies a position of paramount significance. This technology undertakes the analysis of image data via sophisticated algorithms, thereby possessing the ability to automatically discern the position as well as the size of a face. Its core essence resides not merely in determining the

existence of a face within an image, but rather, more pivotally, in accurately and precisely demarcating the specific locus of the face. When juxtaposed with face recognition technology, face detection technology is principally concerned with the exact pinpointing of faces, and conspicuous differences in functionality are manifest between the two technologies.

Face detection is a key step in detecting face feature points and pose estimation when extracting spectacle feature parameters. The process is shown in Figure 1.

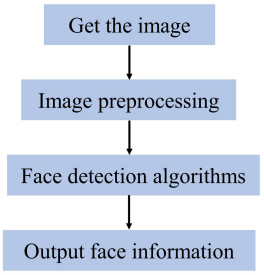

Fig. 1 Facial detection flowchart

At present, there are many different implementations of face pose estimation algorithms [10], including methods based on geometric models, variable templates, appearance models, nonlinear regression, and tracking.

The appearance model amalgamates the shape details and appearance characteristics of the face. It can capture the variation patterns of the face and achieve the estimation of the pose by learning from a substantial amount of training data. This approach detects the positions of feature points by inputting face images. Subsequently, the model parameters are modified to optimally align with the detected feature points, and the pose information of the face, such as rotation and translation, is deduced. Eventually, the estimated face pose information is output. With the AAM template established, the pose of a face can be estimated merely by localizing it and detecting the face landmarks. This method enjoys extensive applications in the domains of face recognition, expression analysis, and virtual reality.

Once the feature points of the face are obtained, the pose of the face can be calculated by combining the 3D face model of the face. In this regard, the POSIT algorithm [11], CV_P3P algorithm [12] or CV_EPNP algorithm [13] implemented in OPENCV can be utilized. These algorithms only need to use the 3D coordinates of a small number of points in the model to accurately calculate the rotation angle and translation distance of the face. At present, our research group has successfully used the face detection method to realize the public invention patent for the collection of facial landmarks.

To enhance the testing efficiency, modifications have been made to the relevant code of the system control logic, while the functional code remains unaltered. The gray box test method is employed. Based on the test data and evaluation metrics, the following test protocol was devised: The pictures in the LFW face database and those containing faces sourced from the Internet were named in numerical increments. There were a total of n pictures, which were loaded one after another, and the feature points were matched. The count of successful matches was designated as x, and the accuracy rate was calculated as x/n. During the actual testing process, 400 images were selected from the LFW face database for loading. The feature points of 391 images were successfully identified and extracted, whereas 9 images could not be accurately identified. Consequently, the accuracy rate was 97.75 percent.

Figure 2 below shows an example of some image matching results. Based on the outcomes of feature point matching, the feature point detection system is capable of aligning the corresponding feature points in accordance with diverse face postures and facial shapes, thereby attaining a satisfactory result. In the illustrated figure, the red-marked segments represent certain face images that have been inaccurately detected. The obstruction of facial features by hair and the absence of prominent mouth characteristics have an adverse impact on face detection, consequently resulting in the failure of feature point identification. In general, the precision of the overall feature point matching remains within the anticipated range.

Fig. 2 Partial matching results of LFW facial database

B. Aspheric lens design theory

Compared to conventional spherical lenses, aspherical lenses can effectively solve the aberration problem and improve the thickness and appearance of the system by reducing the number of lenses. As shown in Figure 3, aspherical lenses have the advantage of significantly improving the focusing performance of the light beam and effectively adjusting spherical aberration, aberration, coma, field curvature, and aberration in light transmission. Simultaneously, the employment of aspherical elements can also enhance the aesthetic appearance of the optical device and streamline its structure, thereby diminishing the overall cost of the system. Consequently, aspherical optical elements have emerged as one of the essential constituents in the production of eyewear, attributable to their remarkable optical properties and the progressively increasing manufacturing precision.

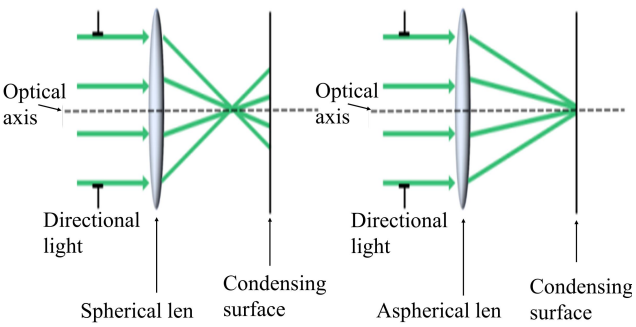

Fig. 3 Focusing effect of spherical and aspherical lenses

An aspherical len is a type of lens possessing a specific radius of curvature and a distinct face shape. In the narrow sense, this concept encompasses mathematical surfaces such as elliptical, hyperbolic, and parabolic ones. At each point on these surfaces, the radius of curvature varies and is defined by a high-order polynomial. In a broader perspective, aspheric lenses refer to any surfaces other than the planar and spherical ones, which also include complex free-form surfaces.

In accordance with the theoretical underpinnings, the category of aspherical surfaces can be segmented into axisymmetric aspherical surfaces and non-axisymmetric aspherical surfaces. Owing to the fact that axisymmetric aspherical surfaces are generally more amenable to design and processing, they hold certain advantages in eradicating dispersion and spherical aberration, and the associated production costs are relatively modest. In contrast, non-axisymmetric aspheres are more appropriate for complex optical systems, yet they are typically more arduous and expensive to fabricate. Consequently, this paper opts for the design of a third-order axisymmetric aspherical surface for the aspherical surface design of spectacle lenses.

Non-axisymmetric aspherical surfaces: common expressions for non-symmetric aspherical surfaces [14] See equation (1):

$$y(x,y)=\frac{C_s z^2}{1+\sqrt{1-(1+k)C_s^2 z^2}}+\sqrt{R_x^2-x^2}-R_X \quad (1)$$

Where x-axis-the long axis of the aspheric lens;
R_x-the base radius of the long axis;
z-axis-the short axis of the aspheric lens;
R_Z-the base radius of the short axis;
y-the coordinate value of the aspherical lens at any point;
R_s-radius of the short axis of the asphere;
k-aspherical coefficient;
A_2, A_4, A_6, A_8, A_{10}, A_{12}-aspherical short axis coefficient;
$C_s = 1/R_s$;
$R_s = -R_Z + A_2 x_2 + A_4 x_4 + A_6 x_6 + A_8 x_8 + A_{10} x_{10} + A_{12} x_{12}$.

Since axisymmetric aspheric surfaces are generally easier to design and machine, they have one in eliminating astigmatism and spherical aberration certain advantages, and the production cost is relatively low. Axially symmetric aspheric surfaces are suitable for complex optical systems. And it is often more difficult and expensive to manufacture. Therefore, a third-order axis is used for the aspherical design of spectacle lenses symmetrical aspheric design.

From a wavefront perspective, an asphere can be understood as a combination of a spherical shape and a nearly infinitely thin correction plate. We are able to determine the desired aspheric shape by finding a curve that matches the optical range difference of a known reference spherical optical system [15]. As a result, sub-aspheric ophthalmic lenses can have a design in which one or both surfaces are aspheric to effectively correct for spherical aberration. Taking the third-order axisymmetric aspheric design [16-17] as an example, assuming that the optical system contains only one aspheric lens, by deriving the Saidel aberration coefficients for an aspheric lens system, we can obtain the aberration coefficients for imaging an object at infinity ($s_1 = \infty$, $h_1 = 1$, $Y_1 = -1$, $\bar{h}_1 = -\bar{s}_1$), see equations (2) to (9):

$$S_I^{asf} = M + \delta M \quad (2)$$

$$S_{II}^{asf} = -\bar{s}_1 M + N - s_1 \delta M \quad (3)$$

$$S_{III}^{asf} = -\bar{s}_1^2 M - 2\bar{s}_1 N + \varphi + \bar{s}_1^2 \delta M \quad (4)$$

$$S_{IV}^{asf} = \varphi / n \quad (5)$$

$$S_V^{asf} = -\bar{s}_1^3 M + 3\bar{s}_1^2 N - s_1(3+1/n)\varphi - \bar{s}_1^3 \delta M \quad (6)$$

$$\delta M = X^3\alpha + 3X^2\beta + 3X\alpha + \beta \quad (7)$$

$$M = \varphi^3(AX^2 - BX + C + D) \quad (8)$$

$$N = \varphi^2(EX - F) \quad (9)$$

Where φ-the degree of the lens;
s_1-the position of the entrance pupil;
n-refractive index of spectacle lenses.

If the lens has only one aspherical surface, Eq. (7) has either.

The first (front) lens surface is aspherical, i.e., b ≠ 0, b'=0, then it remains unchanged, see equation (10):

$$\delta M = \alpha(X^3 + 3X^2 + 3X + 1), b = \frac{8(n-1)^2}{\varphi^3}\alpha \quad (10)$$

The second (rear) lens surface is aspherical, i.e., b'≠0, b=0, holds, see equation (11):

$$\delta M = \beta(-X^3 + 3X^2 - 3X + 1), b' = \frac{8(n-1)^2}{\varphi^3}\beta \quad (11)$$

In addition, φ is applied to the entrance pupil s_1 and the exit pupil $\bar{s}_1$ position, see equation (12):

$$\bar{s}_1 = \frac{\bar{s}_1'}{1 - \bar{s}_1'\varphi} \quad (12)$$

The sum of Seidel coefficients for the spherical aberration of a rotationally symmetric aspherical lens is given here in Eq. (13):

$$S_{III}^{asf} = (\bar{s}_1^2\alpha)X^3 + \bar{s}_1^2(\varphi^3 A + 3\beta)X^2 + \bar{s}_1[\bar{s}_1(3\alpha - \varphi^3\beta) - 2\varphi^2 E]X + \bar{s}_1^2\varphi^3(C+D) + 2\bar{s}_1\varphi^2 F + \varphi + \bar{s}_1^2\beta \quad (13)$$

If we compare the previous relation with that of spherical lenses, we can see that in aspherical lenses with corrected astigmatism ($S_{III}^{asf} = 0$), the real solution always exists because the cubic equation has at least one real root. This means that we are able to make aspherical lenses with better image quality than spherical lenses and can eliminate the spherical aberration caused by spherical lenses. In addition, aspherical lenses can be used to design lenses that are lighter in weight, or correct for other types of aberrations besides astigmatism. It's important to know that a common type of aspheric surface is often needed to correct eye refractive errors better.

C. Parameterization requirements for glasses

By referring to the international parametric standard for spectacle design (GB/T142117003) and other related

national standards (GB13511-2011, GB/T5707010, GB/T2428-1998), the parameter range of spectacle design suitable for individual facial features can be analyzed.

Total frame width: It represents the maximum distance between the left and right endpieces, as illustrated by B in Figure 4 (a). During the design process of the frame's overall width, two crucial factors must be considered. The first one is to guarantee that the frame fits firmly and securely, preventing any potential slippage. The second factor is to steer clear of overly tight squeezing on the head, as this could have a negative impact on the wearing experience. As shown in TABLE I below:

TABLE I
MIRROR FRAME DESIGN DATA REFERENCE RANGE

Range	Frame width
too narrow	128-132mm
narrower	13136mm
moderate	136-140mm
wider	140-144mm
too wide	141648mm

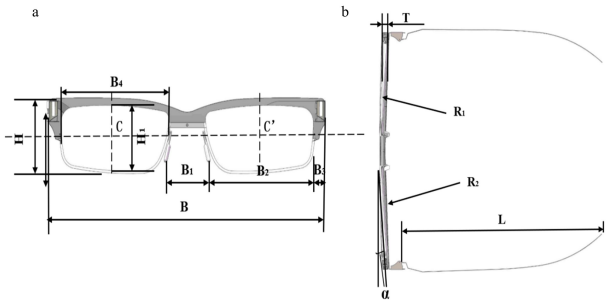

Fig. 4 Eye design parametric diagram

Nose Bridge Width: Refers to the straight-line distance between the horizontal center line of the nose bridge and the intersection points of the edges of both sides, as shown in B1 in Figure 4 (a). When designing the nose pads, factors such as the height and spacing of the nose bridge need to be considered, as there are many acupuncture points and soft tissues at the nose. In general, there will be a difference in the spacing of the nose pads between adults and children. The distance between the nose pads is usually 9.0-10.5mm for children and 12.0-15.2mm for adults.

Rim Width: The farthest distance of the horizontal line of the frame, as shown in B2 in Figure 4 (a). Studies have shown that the width of the lens rim is mainly related to the width of the user's eyelids, so the width of the lens rim should be greater than the width of the eyelids. TABLE II below shows the reference data of the lens rim:

TABLE II
MIRROR CIRCLE RELATED DATA

Range	Rim width
too narrow	42mm
narrower	46mm
moderate	50mm
wider	52mm
too wide	58mm

Pile head width: The horizontal distance between the temples and the bead connection, as shown in B3 in Figure 4 (a). This design parameter has a great impact on the mechanical properties of the glasses, if it is too wide, it is easy to cause the glasses to break, and if it is too narrow, it will affect the aesthetics of the wear.

Rim Height: The farthest distance of the perpendicular line of the rim is shown by H in Figure 4 (a). To maintain aesthetics, the upper edge of the rim should not be too high.

Bridge angle: Usually refers to the angle at which the bridge (the bridge of the frame) fits to the face, which is one of the key factors in ensuring that the glasses fit comfortably on the bridge of the nose. This is shown in Figure 4 (b) in α.

Temple length: The distance between the end of the pile head and the end of the temple (as shown by L in Figure 4 (b)). The length of the temples is related to the distance from the user's eyes to the base of the ear, which is generally 120-150mm for children and 140-170mm for adults.

Lens geometric center: The distance between the midpoints of the left and right lenses. This is shown in C-C' in Figure 4 (a).

Lens height: Lens height refers to the vertical distance of the lens from top to bottom. This is shown in H1 in Figure 4 (a).

Lens width: Lens width is the transverse dimension at the widest point of the lens and is essential to ensure a comfortable fit in the glasses. This is shown in B4 in Figure 4 (a).

Lens thickness: Refers to the thickness of the center of the lens, as shown in T in Figure 4 (b). In general, for aesthetic and easy wearing, the center thickness of the lens should not be too thick.

Radius of curvature of the front and back surfaces of the lens: This primarily relates to the configuration and dimensions of the lens surface, as demonstrated by R1 and R2 in Figure 4 (b). It is defined as the extent from the curved surface of the lens to the center of the circle which is formed by the said surface. It constitutes one of the essential determinants that influence its optical characteristics.

D. DLP 3D printed glasses

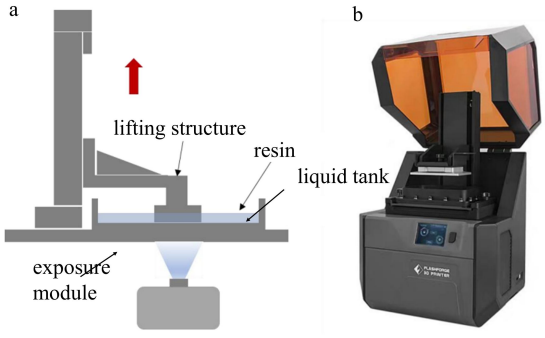

Fig. 5 DLP 3D printing (a) Schematic diagram of DLP 3D printing (b) Physical DLP 3D printer

In order to satisfy the aesthetic and personalized

requisites of patients, the team resorted to a high-precision 3D printing methodology predicated on digital light processing (DLP) for the manufacturing of glasses. Specifically, the spectacle lenses were fabricated with Crys100 highly transparent resin, while the frames were prepared using Rigid series rigid resin (milky) materials.

DLP 3D printing technology harnesses digital light processing technology to harden photosensitive resins and thereby fabricate three-dimensional objects. The process commences by slicing the 3D model. Subsequently, a digital micromirror device (DMD) is deployed to regulate the reflection of the light source (ultraviolet light), precisely illuminating the resin surface and curing it into discrete cross-sections of the model in a single stroke.

As the printing platform advances layer by layer and the resin solidifies incrementally, the entire three-dimensional object is gradually assembled. Thanks to its remarkable speed and high resolution, DLP technology has gained extensive popularity. It is especially adept at manufacturing small and intricate items that necessitate fine and accurate detailing. As depicted in Figure 5, (a) depicts a schematic illustration of DLP 3D printing, and (b) showcases Hunter, a DLP 3D printing apparatus utilized for the production of eyeglasses.

III. Results

A. Spectacle frame modeling design

Glasses mainly comprise frames and lenses. The frame has five key parts: the frame body, two temples, and two connecting rods. Frame customization depends chiefly on the rim's size, realized through its distance and angle parameters. Temple customization, considering individual head differences, is achieved by the distance parameter. As the connecting rod just connects, it doesn't need customization. Frame customization involves parameters like rim width, height, nose bridge width, pile head width, nose bridge angle, and temple length. Once the part sketch is fully defined, a change in main part parameters makes secondary parameters constrain the part, allowing for synchronous update of the glasses part. Shown in Figure 6 is the parametric model of the spectacle frame.

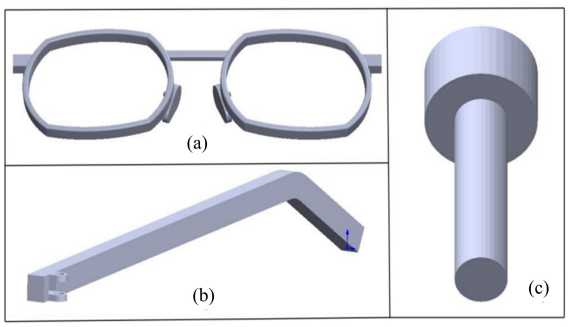

Fig. 6 Parameterized model of eyeglass frame (a) Eyeglass frame (b) Glasses legs (c) Connecting rod

As illustrated in Figure 7, ultimately, upon the full definition of the sketch, a parametric spectacle lens model, which features a third-order axisymmetric aspheric surface on the front of the lens, can be obtained through commands like rotation and cutting. This lays the foundation for the subsequent 3D printing of myopia glasses.

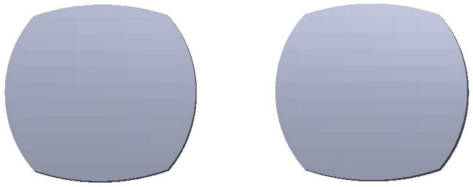

Fig. 7 A parameterized model for non-spherical eyeglass lenses

B. Aspherical modeling design of spectacle lenses

In this article, the ZEMAX simulation software is employed to conduct an analysis of the aberration of aspherical lenses. The aspheric spectacle lenses designed in this paper possess the following initial parameter characteristics as presented in TABLE III. The entrance pupil diameter is measured to be 40 mm. The number of image spaces is 10. The relative aperture is set at 0.1. The full field of view amounts to 10 degrees. Monochromatic light irradiation with a wavelength of 0.6328μm is employed, and the BK7 glass material is adopted. The technical requirements of the system are oriented towards achieving the minimum possible spot. Meanwhile, it is mandatory that the Modulation Transfer Function (MTF) exceeds 0.4 and the aberration remains below 1 percent.

TABLE III
Initial parameters of aspherical lenses

Parameter type	Numerical value
dilation of the pupil of the eye (mm)	40
Like the space F-number	10
full field of view (°)	10
Wavelength (um)	0.6328
makings	BK7

The principal procedures in the design of aspherical lenses are as follows. To commence with, in accordance with the stipulations of Table 6, the initial structure of a single spherical lens can be formulated by configuring the fundamental parameters. The radius of curvature and thickness of surface 1, along with the thickness of surface 2, are designated as variable parameters, and the optimization evaluation function is established as the spot radius. Concurrently, the boundary conditions of the lens are demarcated with a minimum thickness of 2 mm, a maximum thickness of 10 mm, and an edge thickness of 2 mm.

Subsequently, both the evaluation function and the boundary conditions are configured. Given that the design pertains to an aspherical lens, it is requisite to transform surface 1 into an odd-order aspherical surface and augment the conic coefficient ‘k’ as well as the aspherical higher-order coefficients A01 and A03, which are employed as variable parameters for optimization. Eventually, the geometric aberration and transfer function are optimized. When engineering a spherical lens system, the astigmatism and field curvature necessitate minimization, and the spherical aberration is rectified by means of aspherizing surface 1.

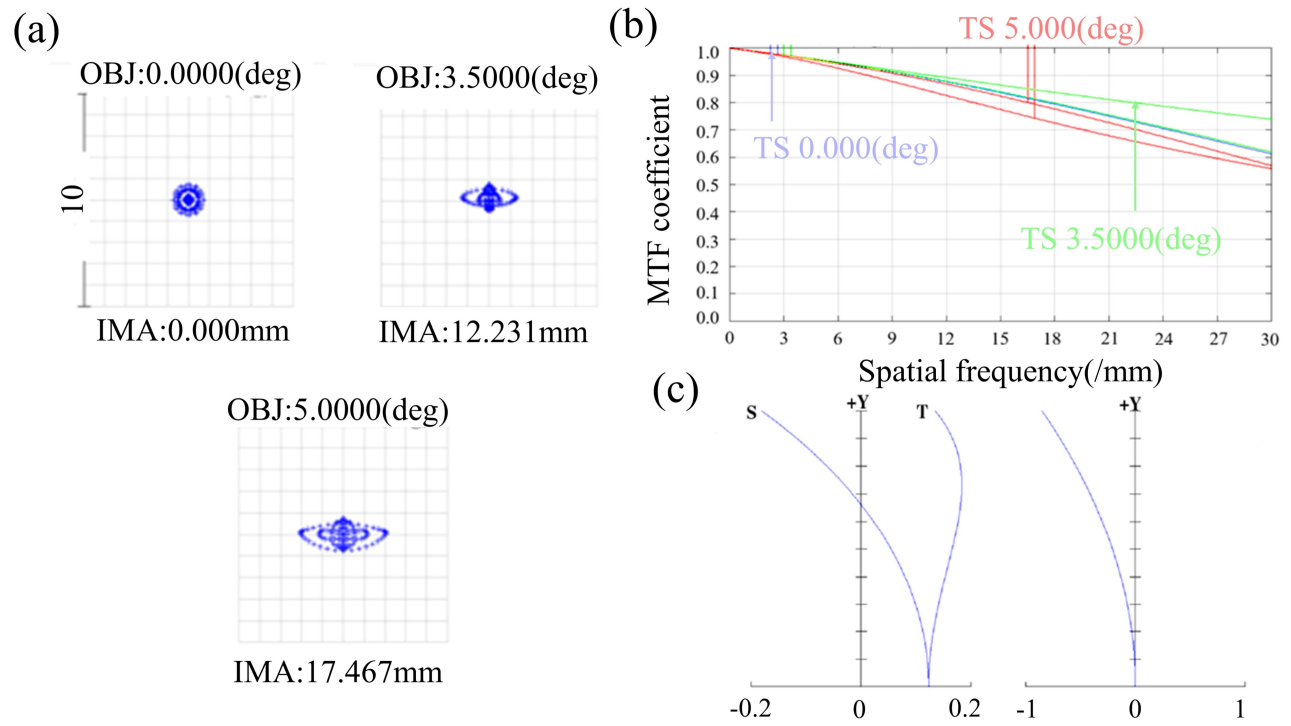

Fig. 10 Aberration Analysis (a) Spot diagram for aspheric spectacle lenses (b) MTF diagram for aspheric spectacle lenses (c) Field curvature and distortion diagram for aspheric spectacle lenses

By optimising the design of the aspherical lens after the previous steps, the resulting third-order axisymmetric aspherical lens parameters are shown in TABLE IV and V:

TABLE IV
DESIGN RESULTS OF ASPHERICAL LENSES

Surf	Radius(mm)	Radius(mm)	Glass
OBJ	Infinity	Infinity	/
STO	Infinity	518.078	/
2 Odd	2669.187	9.940	BK7
asph	/	/	/
3	544.588	195.120	/
IMA	Infinity	/	/

TABLE V
DESIGN RESULTS OF ASPHERICAL LENSES

Surf	Semi-diameter(mm)	conic	Glass
OBJ	Infinity	/	/
STO	10.000	/	/
2 Odd	60.532	3994.775	A_{01}=-2.836×10-5
asph	/	/	A_{03}=-1.115×10-6
3	60.221	/	/

From the simulation outcomes, it is evident that the optimized lens exhibits a substantially reduced thickness. In comparison with the spherical lens of the initial structure, its half aperture has been augmented from the original 16 mm to 60 mm. The central radius of curvature of the aspheric surface is c = -2669.187 mm, the conic coefficient is k = -3994.775, and the third-order coefficients are A_{01} = -2.836×10^{-5} and A_{03} = -1.115×10^{-6} respectively. As depicted in Fig. 8, the diagram of the simulation model obtained through ZEMAX local optimization is presented.

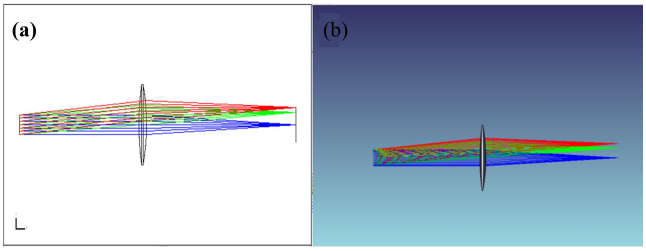

Fig. 8 Non spherical lens model diagram (a)3D layout diagram (b) Shadow pattern diagram

Therefore, the optimal aspherical equation (14) can be obtained through equation (1), substituting the correlation coefficient:

$$Z(x)=\frac{-2669.187x^2}{1+\sqrt{1-(-3993.775)\times(2669.187)^2x^2}}-2.826\times10^{-5}x-1.115\times10^{-6}x^3 \quad (14)$$

C. *Optical performance simulation testing*

The evaluation of the imaging quality of aspheric spectacle lenses consists of: aberration and Seidel coefficients, dot-list plots, modulation transfer functions, field curvature and aberrations.

Within the aspheric spectacle lens Seidel coefficient diagram, as illustrated in Figure 9, it can be discerned that the structural configuration of the entire optical system facilitates the mutual compensation among spherical aberration, coma aberration, and astigmatism. Notably, the spherical aberration has been substantially mitigated. Although a marginal increment in aberration is observed, it remains within the permissible and effective range and thus

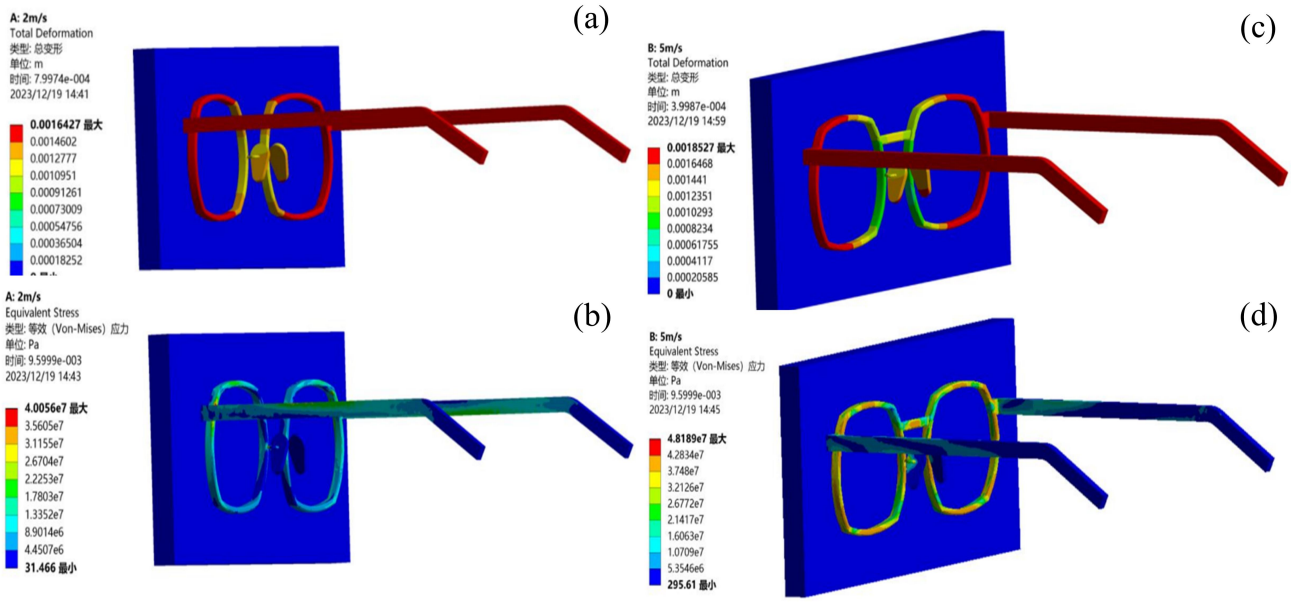

Fig. 11 Diagram of equivalent stress and total deformation resulting from collisions at different velocities (a) Total deformation caused by collision at a speed of 2m/s (b) Equivalent stress generated by collision at a speed of 2m/s (c) Total deformation caused by collision at a speed of 5m/s (d) Equivalent stress generated by collision at a speed of 5m/s

does not exert any adverse influence on the optical imaging performance of the system. Consequently, this leads to the attainment of optimal imaging quality across the entire optical system.

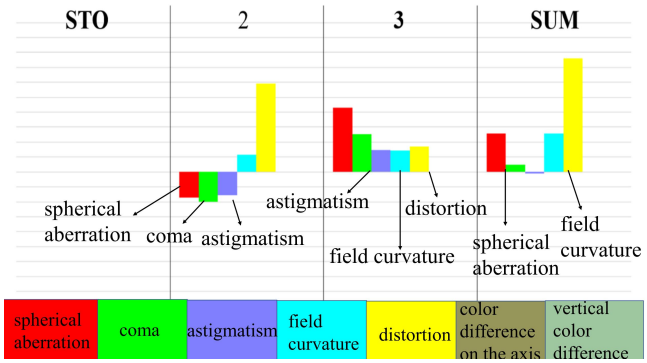

Fig. 9 Seidel coefficient diagram of aspherical eyeglass lenses

As shown in Figure 10, we analyzed the aberrations of the optical system. As shown in Fig. (a), the light spots in the dot-column diagram exhibit symmetrical and concentrated characteristics. In addition, the rms radius of the spot is 5.027 um, 6.049 um, and 9.734 um, while the geometrical radius is 7.200 um, 12.319 um, and 20.085 um at three angles of the Y-axis field of view of 0°, 3.5°, and 5°, respectively, and the airy spot radius of the overall aspherical optical system is 9.275 mm, which indicates that the aspherical system is close to the diffraction limit, which substantially corrects the spherical aberration and improves the imaging quality.

As illustrated in Fig. (b), the blue, green, and red curves respectively signify the Modulation Transfer Function (MTF) coefficient curves in the meridional and sagittal directions corresponding to aspheric spectacle lenses at three distinct fields of view, specifically 0°, 3.5°, and 5°. For the purpose of ensuring precision, a maximum spatial frequency of 30 lp/mm is designated for the solitary lens. Observing from the comprehensive configuration of the curves within the MTF plot, subsequent to the conversion of the initial structure into an aspherical form, the MTF curves exhibit a relatively mild inclination. Concurrently,the area encompassed by the curves at the three fields of view is more extensive. Notably, at the maximum spatial frequency of 30 lp/mm, the MTF value surpasses 0.6, thereby manifesting that the entire optical system attains a relatively satisfactory imaging performance. As demonstrated in Fig. (c), the field curvature of the aspheric spectacle lens optical system fluctuates within a range of 0.2 mm, and the degree of image distortion is exceedingly slight. Moreover, the aberration of the entire system is also confined to less than 1 per cent, and the disparity between the object and the image resides within the admissible error margin.

D. Simulation test of mechanical properties

In accordance with the pre-established initial velocities and termination times, the overall deformation and equivalent stress of the spectacle frame subsequent to its collision with an obstacle can be computed within the realm of explicit dynamics physics. The initial velocities are configured as 2 m/s and 5 m/s respectively, while the termination times are set at 0.075 s and 0.03 s correspondingly. Figure 11 exhibits the comprehensive deformation diagram and stress contour diagram procured by resolving the scenarios involving the two distinct velocities.

According to the results of the simulated contour diagram, after the collision at the initial velocity of 2m/s, the maximum equivalent stress of the spectacle frame is 40.056Mpa, and the maximum deformation is 1.64mm. At an initial velocity of 5m/s, the maximum equivalent stress is 48.189Mpa, and the maximum deformation is 1.85mm.

Subsequent to the post-processing via ANSYS, as illustrated in Figure 12, a collision node is selected within the Z-axis displacement-time graph of the spectacle frame and the obstacle. Irrespective of whether the velocity is 2

m/s or 5 m/s, the overall tendency of the curve is analogous. The displacement progressively augments from zero to a peak value, subsequently diminishes gradually and ultimately attains a stable state. The maximal value herein symbolizes the maximum displacement of the node, whilst the stable value denotes the terminal position of the node. In accordance with the graphical representation, the higher the initial velocity, the briefer the time required for the node to reach its maximum displacement and final position.

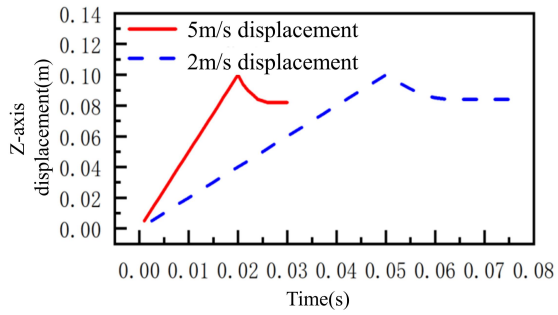

Fig. 12 Displacement time curve of glasses frame collision

According to the ophthalmoscope test requirements, the permissible stress range for the ophthalmoscope is 35 MPa ≤ σ ≤ 103 MPa, and the deformation must satisfy Δl ≤ 2 mm. From the simulation results of the spectacle frame's impact resistance (including the contour diagram and displacement-time curve), at 2 m/s and 5 m/s, the frame's maximum equivalent stress (35 MPa ≤ σ ≤ 105 MPa) and maximum deformation (Δl ≤ 2 mm) meet the standards. Thus, without excessive speed impact, any damage to the glasses won't affect normal use, ensuring the glasses' integrity and user safety.

E. DLP 3D printing parameters

The depth of cure and the molding accuracy are significantly affected by the exposure time and light intensity. The curing depth limits the slice thickness of the computer model, which in turn affects the printing results.

Considering the two influencing factors, two sets of experiments were designed. The low-cost Rigid series rigid resin (amber) was chosen as the test material. The curing depth of printed parts was examined with an exposure time ranging from 1s to 50s and a light intensity of 1.4W to analyze print fineness. The DLP printer's peak power in this experiment was 3.5W. Then, with the exposure time set at 8s and the same test material, the curing depth of printed parts under a light intensity from 0.35W to 3.5W was investigated.

In Figure 13 (A), when the exposure time is 8s, the prints are fully detailed, and the surface is several. There are no defects. In Figure (a), when the exposure time is too short, holes will appear, mainly due to insufficient exposure time, which will cause the resin to not cure sufficiently, resulting in a weak structure. In Figure (c), when the exposure time is too long, more burrs appear around the printed part, and the surface quality of the molded part deteriorates, mainly because the resin is over-cured due to the long exposure time, resulting in distortion or blurring of the fine structure, thus reducing the printing accuracy.

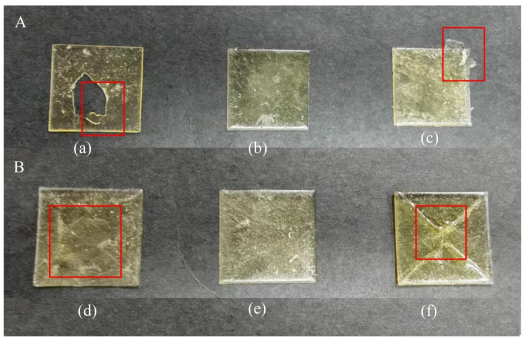

Fig.13 Solidified physical diagram under different conditions (A)Physical images of cured parts with different exposure times: (a) The exposure time is too short (b) The exposure time is 8 seconds (c) Excessive exposure time (B)Physical images of cured parts with different light intensities: (d) The light intensity is too small (e) The light intensity is 1.4W (f) Excessive light intensity

As shown in Figure 13 (B), the physical images of cured parts under different light intensities are presented. In Figure (e), at 1.4W light intensity, the printed parts are fully cured with a uniform and fine surface. In Figure (d), with too low light intensity, the printed part surface is rough and curing is uneven. This is due to incomplete resin curing, leading to insufficient strength. In Figure (f), when the light intensity is too high, the printed part surface is rough and uneven, affecting appearance. This is because excessive light intensity causes rapid over-curing and thermal stress, resulting in deformation.

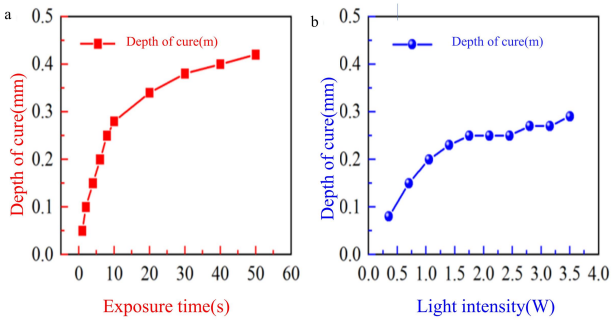

Fig. 14 Results of curing depth with different exposure times and light intensities (a) Effect of exposure time on curing depth (b) Effect of light intensity on curing depth

After importing the data into the Origin software, as illustrated in Figure 14 (a), it becomes evident that an increment in the single-layer exposure time results in a rise in the single-layer curing depth. Typically, the optimal curing depth with a favorable printing effect lies within the range of 0.2 to 0.35 millimeters, and the corresponding exposure time is from 8 to 20 seconds. Therefore, an exposure time of 8 seconds is selected. As can be observed from Figure 14 (b), the curing depth increases in proportion to the light intensity and can reach a maximum of 0.29 millimeters. However, when the light intensity is within the range of 1.4 watts to 3.5 watts, the corresponding curing depth falls within the optimal printing range. Moreover, considering the impact on the printing accuracy of the molded parts, a light intensity of 1.4 watts is determined.

According to the test results, the final printing parameters of the DLP 3D printer were set as follows: the layer thickness was 0.05mm, the bottom layer lifting distance was 5mm, the number of layers was 8, the

exposure time was 8s, and the bottom exposure time was 60s, lifting speed are set at 65mm/min and the light intensity is 1.4W.

Fig. 15 Physical image of glasses

As shown in Figure 15, the actual image of the glasses prepared by setting the parameters of the Hunter DLP 3D printer of Flash casting Technology.

IV. Discussion

A. Quality inspection of Eyewear

In strict accordance with the evaluation methodology specified in the GBT142117003 international standard, a meticulous visual inspection of the spectacle frame surface is carried out without the employment of any auxiliary tools. The exterior of the frame is mandated to exhibit a uniformly distributed color, presenting a smooth and sleek tactile sensation, and being entirely free from any prominent granular defects or blemishes.

TABLE VI
Size comparison results

Measure the object	Theoretical values	Actual	Error
temple length	147mm	147.48mm	0.48mm
lens width	50mm	50.24mm	0.24mm
nose pad width	18mm	17.56mm	-0.44mm

The measurement results of the glasses size are detailed in TABLE VI as follows. It is noteworthy that the measurement precision surpasses 0.5 mm, which adequately meets the necessary and stringent standards.

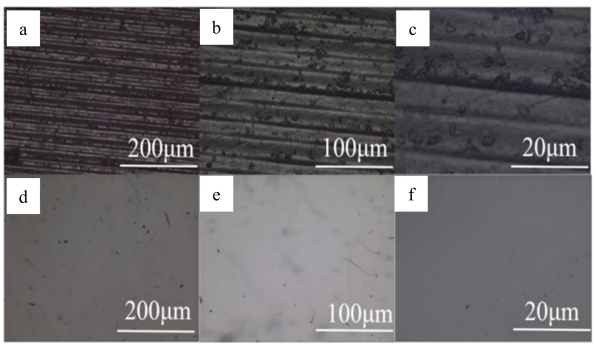

Fig. 16 SEM Results of Unpolished Crys100 High Transparent Resin at Different Scales (a) 50x, (b) 100x, (c) 500x and SEM Results of Polished Crys100 High Transparent Resin at Different Scales (d) 50x, (e) 100x, (f) 500x

As shown in Figure 16, the SEM and 3D topography test results of the Crys100 High Transparency Resin Lens Section are presented. The results are grouped into unpolished (a, b, c) and polished (d, e, f) substrates. The unpolished ones (a, b, c) have an uneven internal structure, surface cracks and defects, and a poor curing effect. In contrast, the polished samples (d, e, f) possess a dense internal structure, no cracks or bubble defects, a flat and smooth surface, sufficient internal curing, and a good curing effect.

Fig. 17 Comparison of different lenses (a) Polished sample (b) unpolished high-transparency resin sample (c) conventional commercial lens sample

In addition, in Figure 17, it can be clearly seen that the light transmittance of the polished lens has been significantly improved. And its light transmittance is not much different from that of general commercial lenses.

Therefore, it was demonstrated from the SEM results that polishing the lens can improve the quality of lens manufacturing, and the process also meets the requirements for the preparation of lens substrates.

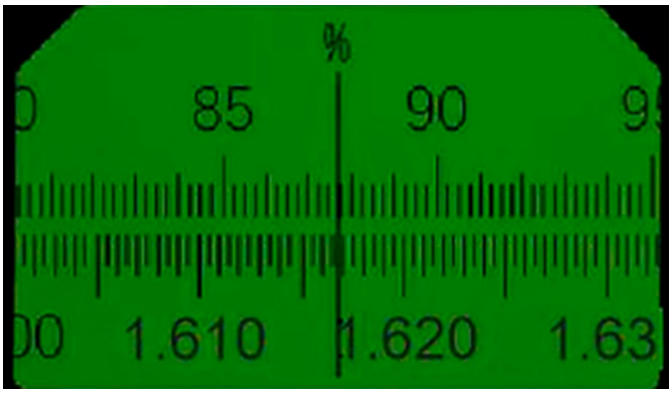

Fig. 18 The refractive index of high-transparency resin sample

The performance of a lens is chiefly shaped by its refractive index. This crucial index functions in a highly intricate manner. As light rays traverse the lens, the refractive index precisely guides their refraction. Moreover, it is directly linked to the lens's thickness. A change in refractive index can thus significantly impact the overall optical functionality, dictating how well a lens focuses and transmits light.

The Abbe number plays a critical role in determining whether unwanted chromatic aberrations, such as rainbow streaks, will occur under certain conditions, thereby impacting the visual experience. Tests conducted on high-transparency resin samples yielded a refractive index of 1.616 and an Abbe number of 36, as illustrated in Figure 18. These results demonstrate that the refractive index of the high-transparency resin lens substrate meets the criteria for high-refractive-index lenses, while the Abbe number adheres to the national standard requirements for lenses, which specify a refractive index (n) greater than 1.60 and an Abbe number (ν) of at least 30. (n>1.60, $\nu \geq 30$)

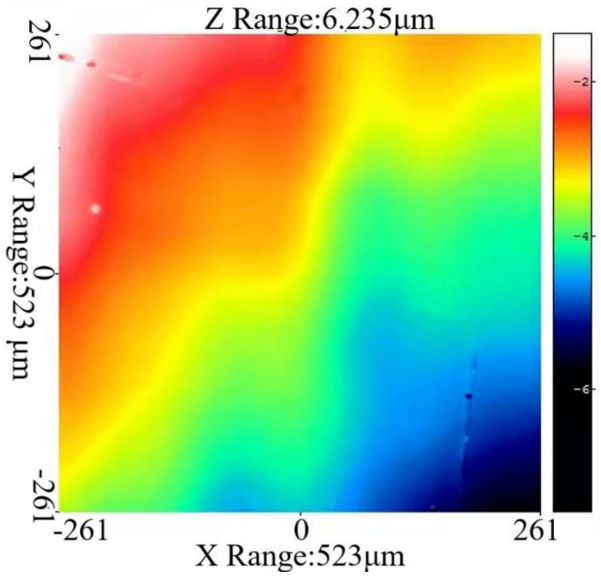

Fig. 19 Surface Concave and Convex Error Results of Crys100 High Transparent Resin Samples

Figure 19 shows a 3D profile of a polished Crys100 highly transparent resin sample surface using the WYKO/NT9100 optical profiler.

In accordance with the results of the three-dimensional contour diagram, the concave-convex error on the surface of the lens is within 6μm. The curvature of the lens is smooth, and there are virtually no conspicuous microcracks, particles or other defects on the surface. Consequently, the DLP 3D printed Crys100 highly transparent resin lenses meet the requirements of the national reference standard QB/T 2506-2017, in which the concave-convex error of the lens is stipulated to be no more than 10μm. Additionally, the color distribution on the lens surface exhibits a gradient effect, indicating that the surface flatness of the lens substrate is satisfactory and satisfies the preparation requirements of the lens substrate.

As illustrated in Figure 20, T1, T2, and T3 correspond to the polished Crys100 high-transparency resin sample, the unpolished Crys100 high-transparency resin sample, and the PMMA material sample respectively.

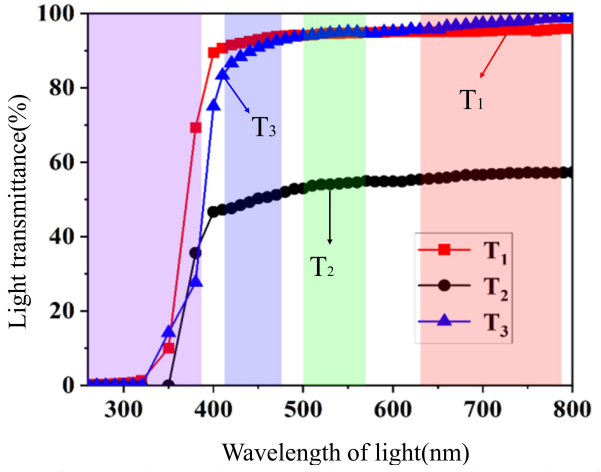

Fig. 20 The transmittance of Crys100 high transparent resin samples and PMMA material samples, both polished and unpolished

As is clearly observable in Figure 20, the transmittance of the PMMA material approximates 97% within the visible light spectrum (ranging from 420 nm to 780 nm for the red, green, and blue wavelengths as illustrated in the figure). The transmittance values of the polished Crys100 specimen in the red, green, and blue wavelengths are in close proximity to those of the PMMA specimen, attaining a level of 94%. In contrast, the unpolished Crys100 specimen exhibits a significantly lower transmittance of only 51%.

The reason for this disparity lies in the fact that the surfaces of unpolished lenses typically possess regions of roughness, pits, scratches, or other forms of unevenness. When light traverses through such lenses, these surface imperfections can lead to the scattering, reflection, or absorption of light, consequently diminishing the overall light transmittance.

Furthermore, it is noteworthy that the Crys100 High Transparency Resin demonstrates an almost negligible transmittance to ultraviolet light. This characteristic implies that it possesses a certain degree of absorptive capacity with respect to ultraviolet light, thereby endowing it with the potential to safeguard the eyes. According to the stipulations of the GB10810-2005 standard, spectacle lenses are mandated to possess a minimum light transmittance of 85%. Given that the Crys100 High Transparency Resin can achieve a transmittance of 94%, it can be conclusively stated that it satisfies the essential requirements for the fabrication of spectacle lenses.

B. Eyewear comfort test

The comfort of glasses is of utmost importance to the user. Specifically, the design and size of the spectacle frame play a vital role. If the design is improper or the size is incorrect, it can cause a suboptimal fit of the glasses on the face and an unequal distribution of pressure. This, in turn, may lead to uncomfortable wearing experiences, pain, or other forms of discomfort. Therefore, the evaluation of comfort in spectacles primarily focuses on the spectacle frame.

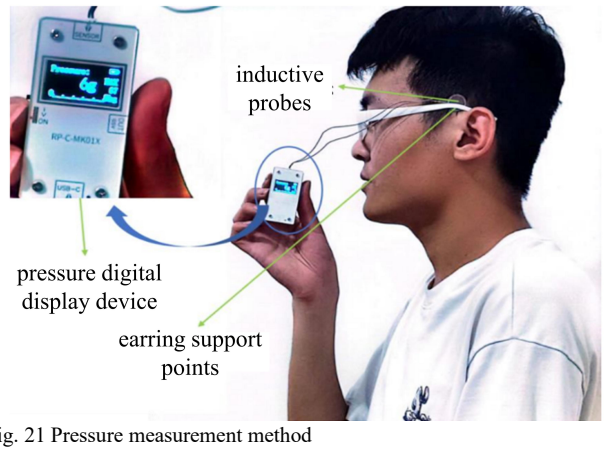

Fig. 21 Pressure measurement method

By affixing the sensor probe of the sensor pressure testing apparatus to the earring support point of the glasses, as illustrated in Figure 21, the corresponding pressure manifestation can be exhibited subsequent to the user donning the glasses.

Figure 22 shows the pressure results at 15 different points of the user obtained by the sensor pressure test setup.

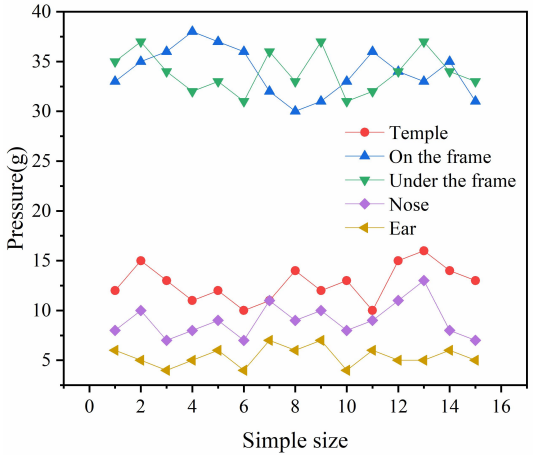

Fig. 22 Pressure refraction diagram of different parts

The eyewear pressure standard demands the temple support point pressure be 10-20g, frame's upper and lower support points 30-50g, nose pad support point 5-15g, and earring support point 12g. Analyzing data from 15 users' tests, the frame's upper/lower and temple support point pressures are higher for a close, stable fit without over-compressing skin. The nose pad pressure is slightly more than at earrings as the nose bridge is the main support and earrings for holding. Averaging the nose bridge and five ear support points' pressures of 15 users meets the ASTM F2802 standard. Thus, the DLP 3D printed eyewear by the custom system fulfills ergonomics and comfort requirements.

C. Vision correction test

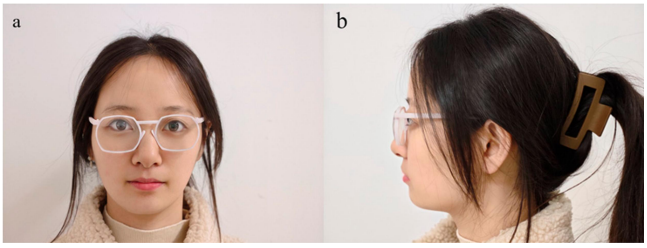

Fig. 23 Wearing 3D printed glasses (a) Main view (b) Side view

As shown in Figure 23, it shows the wearing of 3D printed glasses. In order to evaluate the helpful effect of 3D printed glasses on the correction of myopia, 30 volunteers were recruited to participate in the correction experiment.

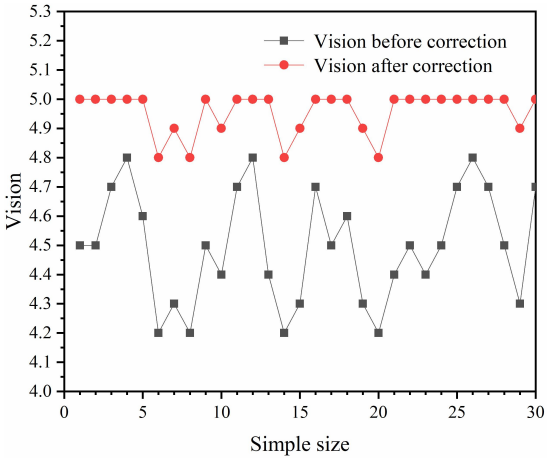

Fig. 24 Comparison of visual acuity before and after correction

Figure 24 shows a comparison of vision correction. After refraction of the volunteers wearing 3D-printed glasses, most of them had their vision back to normal. The remaining volunteers are highly myopic and have a certain degree of astigmatism, and their vision after wearing 3D printed glasses does not affect their normal life.

V. Conclusions

This paper mainly proposes solutions to the problems in spectacle frame structure, lens power, and production. Based on their vision, patients can determine the curvature radii of the lens' front and back surfaces for diopter matching. This reduces spherical aberration's impact and improves optical properties. In addition, the glasses printed via DLP 3D printers meet international optical and mechanical property requirements. To meet quality and comfort demands, they adhere to relevant glasses manufacturing standards, solving material waste and enhancing wearing comfort. Achieving fine customization of lens power, they also address vision loss and eye fatigue from wearing glasses, providing a potential way to improve vision correction in both adults and children later.

Acknowledgment

The authors would like to thank the corresponding author for supervising the study and the other members of the group for their help.

References

[1] I. G. Morgan, A. N. French, R. S. Ashby, X. Guo, X. Ding, M. He and K. A. Rose, "The epidemics of myopia: aetiology and prevention," *Progress in Retinal and Eye Research*, vol. 62, pp131649, 2018.

[2] M. A. Bullimore and N. A. Brennan, "Myopia control: why each diopter matters," *Optometry and Vision Science*, vol. 96, no.6, pp46965, 2019.

[3] B. A. Holden, T. R. Fricke, D. A. Wilson, M. Jong, K. S. Naidoo, P. Sankaridurg and T. Y. Wong, "Global prevalence of myopia and high myopia and temporal trends from 2000 through 2050," *Ophthalmology*, vol. 123, no.5, pp1036-1042, 2016.

[4] T. Xu, B. Wang, H. Liu, H. Wang, P. Yin, W. Dong, J. Li, Y. X. Wang, M. Yusufu, P. Briant and N. Reinig, "Prevalence and causes of vision loss in China from 1990 to 2019: findings from the global burden of disease study 2019," *Lancet Public Health*, vol. 5, no.12, ppe682-e691, 2020.

[5] Y. W. Yu, J. Y. Wang, Y. P. Song, and L. L. Zhao, "Stability analysis of power bogie system and forward design of its yaw damper damping parameter," *Engineering Letters*, vol. 31, no.4, pp14316441, 2023.

[6] D. Tang, J. Zhang, K. Tang, L. Xu and L. Fang, "Making 3D eyeglasses try-on practical," *International conference on multimedia and expo workshops*, IEEE, 2014, pp1-6.

[7] P. Azevedo, T. D. Santos and E. D. Aguiar, "An augmented reality virtual glasses try-on system," *Symposium on Virtual and Augmented Reality*, IEEE, 2016, pp1-9.

[8] Z. Feng, F. Jiang and R. Shen, "Virtual glasses try-on based on large pose estimation," *Procedia computer science*, vol. 131, pp226-233, 2018.

[9] H. Fordell, K. Bodin, G. Bucht and J. Malm, "A virtual reality test battery for assessment and screening of spatial neglect," *Acta neurologica Scandinavica*, vol. 123, no. 3, pp167-174, 2011.

[10] L. Vincenzi, F. Ponsi, E. Bassoli and N. Buratti, "A computationally efficient procedure for calibrating model parameters of multiple specimens," *Construction and Building Materials*, vol. 441, pp134757, 2024.

[11] R. Usamentiaga and D. F. García, "Multi-camera calibration for accurate geometric measurements in industrial environments," *Measurement*, vol. 134, pp345-358, 2019.

[12] Y. S. Phang and Y. Zhao, "Determining the focal length of converging and diverging lenses using a smartphone," *The Physics Teacher*, vol. 60, no. 8, pp701205, 2022.
[13] K. M. Chang, J. L. Cheng and Y. T. Liu, "Machining control of non-axisymmetric aspheric surface based on piezoelectric fast tool servo system," *Precision Engineering*, vol. 76, pp160-172, 2022.
[14] K. Khan, R. U. Khan, R. Leonardi and P. Migliorati, "Head pose estimation: A survey of the last ten years," *Signal Processing: Image Communication*, vol. 99, pp116479, 2021.
[15] D. F. DeMenthon and L. S. Davis, "Model-based object pose in 25 lines of code," *International Journal of Computer Vision*, vol. 15, no. 1-2, pp12641, 1995.
[16] X. S. Gao, X. R. Hou, J. Tang and H. F. Cheng, "Complete solution classification for the perspective-three-point problem," *Transactions on Pattern Analysis & Machine Intelligence*, vol. 25, no. 8, pp930-943, 2003.
[17] V. Lepetit, F. Moreno-Noguer and P. Fua, "EPnP: An accurate o(n) solution to the pnp problem," *International Journal of Computer Vision*, vol. 81, no. 2, pp155-166, 2009.